COMPARISON OF ORBITER PRCS PLUME FLOW FIELDS USING CFD AND MODIFIED SOURCE FLOW CODES

Wm. C. Rochelle,* Robin E. Kinsey,** and Ethan A. Reid**
Lockheed Martin, Houston, TX

Phillip C. Stuart+ and Forrest E. Lumpkin+
NASA/JSC, Houston, TX

Abstract

The Space Shuttle Orbiter will use Reaction Control System (RCS) jets for docking with the planned International Space Station (ISS). During approach and backout maneuvers, plumes from these jets could cause high pressure, heating, and thermal loads on ISS components. The object of this paper is to present comparisons of RCS plume flow fields used to calculate these ISS environments. Because of the complexities of 3-D plumes with variable scarf-angle and multi-jet combinations, NASA/JSC developed a plume flow-field methodology for all of these Orbiter jets. The RCS Plume Model (RPM), which includes effects of scarfed nozzles and dual jets, was developed as a modified source-flow engineering tool to rapidly generate plume properties and impingement environments on ISS components. This paper presents flow-field properties from four PRCS jets: F3U low scarf-angle single jet, F3F high scarf-angle single jet, DTU zero scarf-angle dual jet, and F1F/F2F high scarf-angle dual jet. The RPM results compared well with plume flow fields using four CFD programs: General Aerodynamic Simulation Program (GASP), Cartesian (CART), Unified Solution Algorithm (USA), and Reacting and Multi-phase Program (RAMP). Good comparisons of predicted pressures are shown with STS-64 Shuttle Plume Impingement Flight Experiment (SPIFEX) data.

Introduction

In May 1998 the first segment of the International Space Station (ISS), the Russian Functionalni Gruznoi Blok (FGB), is scheduled to be launched. About 5 years later, the entire 110 m x 75 m x 40 m ISS will be completely assembled. During build-up of this space station, Orbiter Primary and Vernier Reaction Control System (PRCS and VRCS, respectively) jet plumes will impinge upon ISS components while the Orbiter is docking, possibly causing high pressure and heating environments on critical components. One such build-up configuration is seen in Fig. 1 which shows the Orbiter docking at Pressurized Mating Adapter (PMA)-2 during ISS Flight 6A. High impingement environments could arise with the F1F/F2F plume impinging on the bottom of the P6 +x radiator or the F3U plume impinging on the P6 solar array and the Space Station Remote Manipulator System (SSRMS).

The methodology for evaluating Orbiter plumes and impingement effects on both Mir Space Station and ISS components has been underway at NASA/JSC for the past three years. This includes plume flow-field characteristic tests in the JSC Chamber A vacuum chamber[1,2] and development of the RCS Plume Model (RPM)[3-5] and the higher-fidelity CFD/DSMC model.[6] For validation of the analytical models, plume impingement pressure, force, and heat flux data was obtained from Orbiter RCS jet firings from Shuttle Plume Impingement Flight Experiment (SPIFEX).[7-9]

Plume impingement heating environments to specific ISS components have been presented recently.[10,11] An updated plume heating model for the continuum regime was presented a few months ago[12] using the plumes discussed in the present paper. These heating environments were shown to vary as a function of distance between ISS docking ports, location in Orbiter approach cone, location along component, radius of component, and for solar arrays, the array feather angle.

The present paper focuses on the plume flow-field properties used to obtain the heating environments. These plumes were generated by both the engineering model (RPM) as well as by more exact CFD solutions. The remainder of the paper will include a description of the Orbiter jet locations and the PRCS jet coordinate system. A discussion of the SPIFEX configuration on which plume flow field and heating models were validated is also described. The flow-field methodology of the five types of plume programs considered will be briefly summarized, and results, including flow-field property contours and comparisons of properties between the methods, will be presented. In addition, comparisons of impingement pressure with SPIFEX data at the location of specific test points will be given.

*Group Lead, Advanced Systems Group
**Cooperative Engineering Student, Adv. Sys. Grp.
+Aerospace Engineer, Aeroscience Branch

Orbiter Jet Locations and PRCS Coordinate System

A sketch of the Orbiter RCS jet locations and plume centerline firing directions is presented in Fig. 2. There are 38 870-lb thrust PRCS jets and six 24-lb thrust VRCS jets on the Orbiter (all using N_2O_4/monomethyl hydrazine as the propellant), as seen in this figure. Several of the PRCS jets on the forward module have a large scarf angle to conform to the contour of the Orbiter. These include the forward-firing jets (F1F, F2F, and F3F) with a nominal scarf angle of 65° and the downward-firing jets (F1D-F4D) with a nominal scarf angle of 59°. The upward-firing PRCS jets in the forward module (F1U, F2U, and F3U), together with two of the side-firing jets in this module (F1L and F2R) have a nominal scarf angle of 23°. The other two side-firing PRCS jets on the forward module (F3L and F4R) and the left and right-firing jets on either side of the tail (L1L-L4L and R1R-R4R) have a nominal scarf angle of 16°. The up-firing, down-firing, and aft-firing PRCS jets in the aft module all have a zero scarf angle.

The principal PRCS jet used for docking maneuvers is the F3U single jet. Whenever the forward-firing jets are used, they always fire together, producing the F1F/F2F dual-jet plume. Also, the up-firing, down-firing, or aft-firing jets on either side of the vertical tail fire together (e.g., R1U/L1U), producing a dual-jet plume. When the up-firing jets fire, this is referred to as the Dual-Tail-Up (DTU) jet. In addition, if the F3U jet fires while the DTU jet is firing, the jets fire in the "norm-z" mode with three intersecting plumes.

In Fig. 3, the Orbiter PRCS coordinate systems are shown for: (a) the single-jet, unscarfed nozzle; (b) the dual-jet, unscarfed nozzle; (c) the single-jet scarfed nozzle; and (d) a schematic of the Orbiter forward module showing the multiple-jet scarfed nozzles. From these figures, the scarf angle, ξ; distance, r, from nozzle exit to an object in the plume; azimuth angle, θ, from the centerline; clock angle, ϕ, around the nozzle; and thrust vector angle, ψ, may be seen.

SPIFEX Configuration

Figure 4 presents a sketch of the equipment used for the SPIFEX operation. The experiment arm was mounted at the end of a 10-m long boom which was attached to the end of the Shuttle Remote Manipulator System (RMS). This figure shows the general position of the arm above the F3U jet plume. Two plates were on the experiment arm containing instrumentation - Load Measuring System (LMS) plate and Plume Impingement Characterization System (PICS) plate. Four heat flux sensors were on the LMS plate and three on the PICS plate. The PICS plate contained four pressure sensors (absolute and differential capacitance manometers and Sentran and Kistler gages). Pressure measurements could also be deduced by dividing the force measurement by the plate area. This SPIFEX data will be compared with impingement pressures obtained from plume flow fields discussed below.

Plume Flow-Field Methodology

This section discusses the plume flow-field methodology for the RPM code[3,4] and the CFD programs: General Aerodynamic Simulation Program (GASP),[13] Cartesian (CART) code, Unified Solution Algorithm (USA)[14] program, and the Reacting and Multi-phase Program (RAMP).[15] Plume runs were made with the RPM, GASP, CART, and RAMP codes, while the results of the USA code were furnished by Rockwell.[14] The F3U plume was generated by the RPM, GASP, and RAMP codes, the F3F plume was run for the RPM and GASP codes, the DTU plume was predicted by RPM and GASP, and the F1F/F2F plume was generated by RPM, CART and USA.

RPM

The RPM code uses modified source flow relations to predict plume dynamic pressure for a nozzle for a given value of ξ as a function of r, θ, ϕ, chamber pressure, ratio of specific heats, combustion efficiency, and limiting streamline angle. The relation between distances and angles is seen in Fig. 3. In RPM, the plume velocity is constant with azimuth angle in the inviscid core until the limiting streamline is reached, which divides the inviscid core and viscous boundary layer. The velocity decreases across the boundary layer to account for energy losses. Inside the shock interaction region of dual-jet plumes, RPM dynamic pressures are amplified by factors obtained from fits of CFD and DSMC solutions for the DTU plume. For the F1F/F2F plume, RPM dual-jet amplification factors were further adjusted based on SPIFEX data. The RPM model uses velocity and static pressure curve fits in the shock interaction region to envelope the region predicted by the CFD solutions (described below).

GASP and CART

The GASP code was used for the nozzles and plumes of the F3U zero scarf-angle (axisymmetric) jet, the F3U 22.7° scarf-angle jet, the F3F 65.0° scarf-angle jet, the

zero scarf-angle DTU jets, and the nozzle of the 64.8° scarf-angle F1F/F2F dual jet. Because of the extreme scarf angle coupled with the proximity of the nozzles to the Orbiter centerline, problems occurred in producing a grid of adequate quality using GASP for the F1F/F2F plume. Thus, the JSC CART code, a purely Cartesian flow solver that automatically clusters grid points to gradients in the flow field, was used for this plume.

The thin-layer Navier-Stokes equations were solved with the Baldwin-Lomax[16] turbulence model using a 500 K constant wall temperature. A finite-rate chemistry model with eleven species (CO, H_2, N_2, NO, O_2, OH, CO_2, H_2O, H, N, and O) was used with 86 reactions and vibrational equilibrium. By the time the flow had reached the nozzle exit, it was chemically frozen; hence, in the plume, the chemical reactions were disabled, and the flow was frozen along streamlines.

The initial conditions in the combustion chamber using GASP were based on results of the NASA/Lewis Chemical Equilibrium Composition (CEC) code[17] with a 2-temperature range curve-fit inside the nozzle and a single harmonic oscillator model in the plume for the thermodynamic properties. The flow solver used a Roe-averaging 3rd-order Monotone Upstream-centered Scheme for Conservation Laws (MUSCL) technique.[18] The models used with the CART plume solution were similar to those used with GASP in the plume, except that the Van Leer[19] flux calculation was used.

USA

With the USA code, the Navier-Stokes equations were solved with a finite volume scheme (same as with GASP). These equations result in five independent variables for 3-D calculations and four variables for axisymmetric/2-D calculations. The same 11 species and 86 reactions as used by GASP were used with the USA code with finite-rate chemistry in the nozzle and frozen flow in the plume. A modified Baldwin-Lomax turbulence model was used for the flow inside the axisymmetric and scarfed nozzles. For plume calculations with single and dual scarfed nozzles, the USA code used second-order accuracy (while the GASP code used third-order accuracy). The USA code used a 1-temperature curve-fit for thermodynamic properties for both the nozzle and plume. For the scarfed nozzle, the USA code had a 65° inclined plate blending into the Orbiter contour and turning 90° downward at the nose. This was in contrast to the 65° continuous flat plate for the CART and GASP solutions which did not follow the contour of the Orbiter near the nose. The flow-field output of the USA code was in Plot3d[20] format. However, to be compatible with the CART solutions, the Plot3d format was changed to Tecplot[21] format.

RAMP

The RAMP nozzle and plume code has the capability to run a reacting, 2-phase (gas-particle) solution using a shock-capturing finite-difference numerical operator with a variable oxidizer to fuel (O/F) distribution. For the axisymmetric PRCS solution for the F3U jet, an equilibrium/frozen single-phase (gas only) solution was used with the flow chemically frozen along streamlines downstream of the throat (similar to the GASP and USA solutions). A transonic solution with the wall geometry input both upstream and downstream of the throat, including throat radius of curvature, was used. A variable O/F ratio distribution was assumed in the nozzle and plume with an 11-point variation from O/F = 2.2 along the nozzle centerline to O/F = 0.8 at the wall where the MMH fuel is dumped.

The NASA/Lewis CEC code[17] was run initially to obtain thermochemical properties for the RAMP nozzle solution. Then RAMP was run for inviscid flow inside the nozzle. The Boundary Layer Integral Matrix Procedure - Version J (BLIMPJ) code[22] was then run inside the nozzle to obtain the viscous boundary layer flow including displacement thickness along the wall. An assumed wall temperature distribution varying from 1303 K at the throat to 1234 K at the exit plane (0.236 m from the throat) was used. The RAMP code was then run for a modified nozzle wall with the BLIMPJ displacement thickness subtracted off the wall. The BLIMPJ code was run a second time to further adjust the wall boundary layer, and a combined inviscid/boundary layer start line at the exit plane was used for input to the RAMP plume run. This axisymmetric plume was thus used for the F3U plume comparison with RPM and GASP solutions.

Results

Plume Flow-field Contours

Figure 5 presents RPM-predicted dynamic pressure contours for the F3U single-jet plume with a 22.7° scarf angle as a function of distance along the Z-axis. In Fig. 5 (a) the contours are shown for the X-Z plane, and in Fig. 5 (b), they are shown for the Y-Z plane. It is seen that the X-Z plane contours are symmetric with respect to the X = 0 axis, while in Fig. 5 (b), the Y-Z contours are shifted slightly downward. Because of the closeness

of the flow-field properties in the two planes, properties from this RPM plume were compared with those of axisymmetric GASP and RAMP plumes. In Fig. 5 (b) several of the SPIFEX test points are shown, at which measured impingement pressures were used to compare with predicted values (discussed later).

In Fig. 6 the dynamic pressure contours are presented for the DTU dual-jet plume as computed by the RPM code. The X-Z view of Fig. 6 (a) shows the shock-interaction region in between these jets, the axes of which are separated by a distance of 6.8 m. The Y-Z view of Fig. 6 (b) shows a stagnation region, but not a shock interaction region. No significant SPIFEX data was taken for this plume.

Figure 7 presents the RPM contours of dynamic pressure for the F1F/F2F dual-jet plume. In Fig. 7 (a) the X-Z view shows the shock interaction region between these jets, the axes of which are separated by a distance of only 0.74 m. The effect of the high scarf angle may be seen in Fig. 7 (b) showing the thrust vector sloping downward to the right. In this plot, the actual Y-axis is the negative value of that shown in Figs. 3 (c) and 3 (d) such that the thrust vector is sloping upward, away from the Orbiter body. Several SPIFEX test points are also shown in this figure.

In Figs. 8 and 9 the RAMP and GASP F3U axisymmetric PRCS plume dynamic pressure contours are shown, respectively. A continuum flow line limits the GASP solution to about Z = 18 m on the axis. It is seen that the contour values are fairly close between the GASP and RAMP values, especially along the axis and compare well with the RPM contours in Fig. 5 (as discussed later). The presence of a reflected shock may be seen in both the RAMP and GASP plots.

Figure 10 presents the DTU plume contours of dynamic pressure in the Y-Z plane as computed by the GASP code. This plot represents a cut across the plume in the Z-direction at 12 m. The shock contour is shown in this figure, with a minimum value at Y = 0, increasing in the X-direction for higher values of Y. This dual-jet plume has two unscarfed nozzles; hence, the flow variables for Y < 0 are the same as those for Y > 0. The center of a single jet may be seen at X = 3.4 m. The shock location compares favorably with that of the RPM DTU plot of Fig. 6 at the same location.

In Figs. 11, 12, and 13, F3F single-jet and F1F/F2F dual-jet plume contours are shown of density, velocity, and molecular weight, respectively, at Z = 2.0 m as a function of Y and X. The contours were computed by GASP for the F3F jet and by CART for the F1F/F2F jet. Both jets have the same high scarf angle (65°), and the F3F jet axis has been shifted over to X = 0.37 m to put it at the same location as the axis of one of the F1F/F2F jets. Figure 11 shows the shock location of the F1F/F2F dual jet which has a similar pattern to that of the DTU dual jet shown in Fig. 10. However, the F1F/F2F contours are not symmetric with respect to the Y = 0 axis like those of the DTU contours because of the high scarf angle of the F1F/F2F jet. The contours in Figs. 12 and 13 show the maximum values of velocity and molecular weight occurring at the axis (X = 0.37 m). In all three figures, the contours of the F3F and F1F/F2F plume (outside the shock) are comparable, in spite of the difference in the two codes.

Distribution of Flow Properties

In Fig. 14 the distribution of the F3U dynamic pressures along the plume axis is shown with a comparison of the RPM, RAMP, and GASP results interpolated from Figs. 5, 8, and 9, respectively. For values of Z > 1 m, the RPM dynamic pressures are slightly lower than the GASP values, which are slightly lower than the RAMP values. The RAMP and GASP curves show a shock structure for Z < 0.5 m (also seen in Figs. 8 and 9, respectively). This shock structure cannot be obtained from the RPM code since it is a modified source-flow code, and its solution actually starts at Z = 1 m.

The distribution of dynamic pressures across the F3U plume computed from GASP, RAMP, and RPM solutions is shown in Fig. 15 at Z = 10 m from the exit plane. All three predictions are close at low values of Y, with a deviation occurring at larger values of Y where the plume is more rarefied.

Figure 16 presents the GASP and RPM distribution of density across the F3F plume in the X-direction at Z = 12.5 m and Y = 1.0 m. The GASP and RPM values are very close for Z < 2 m, with GASP values above those of RPM from 2 to 9 m. The trend reverses itself at larger values of X. In Figs. 17 and 18, the GASP and RPM dynamic pressure and velocity distribution around the F3F plume is shown as a function of clock angle, ϕ, at Z = 12.5 m and θ = 36°. It is seen that the dynamic pressures are fairly close between the two methods, and the velocities are very close.

Figure 19 presents a comparison of density from the DTU plume as a function of X at Z = 18 m from the exit. It is seen that the RPM-predicted location of the

dual-jet shock at X = 1.7 to 2.2 m is very close to the prediction from GASP. The GASP values of density are slightly higher than those of RPM inside the shock and are slightly lower than those of RPM outside the shock (for X > 2.2 m).

In Fig. 20 the dynamic pressures from the CART, USA, and RPM codes are plotted for the F1F/F2F dual-jet plume as a function of Z along the X-Z plane of symmetry. All three of the curves are fairly close for Z > 2 m, with RPM generally the highest. There is a large difference between RPM and both CART and USA for Z < 2 m; however, no component of the ISS would be within 3 - 4 m of the exit of this plume because of the high heating rates at this distance.[11] In the range of Z from 9 - 15 m, all three methods show very good correlation with SPIFEX data (described below).

Figure 21 shows a distribution of dynamic pressure across the F1F/F2F plume at Z = 2 m vs. X using CART, USA, and RPM. The CART and USA values are close inside the shock (X < 0.5 m), while the RPM predictions are generally in between the USA and GASP values for X > 1.5 m. In Fig. 22 a comparison of CART and RPM dynamic pressure for the F1F/F2F plume at Z = 5.0 m is shown as a function of Y along the plane of symmetry. The CART values are slightly higher than those of RPM except for Y < -4 m where the two methods are very close. The CART flow field was terminated for values of Y > 2.3 m.

SPIFEX Data Comparisons

Figure 23 presents a bar chart showing the comparison of impingement pressures measured by SPIFEX for the F3U jet with RPM, RAMP, and GASP predictions. In this and the next two figures, the SPIFEX pressures are the measured loads divided by the area of the LMS plate. Distances from the nozzle exit plane to the sensor, r, of 12.2 to 23.2 m are included in Fig. 23 at nominal azimuth angles, θ of 2° and 15°. The RPM values show excellent agreement with data. The RAMP and GASP values are slightly higher than the data. These impingement pressures are computed by adding the static pressure to the product of pressure coefficient times dynamic pressure. For GASP and RAMP, the pressure coefficient was taken to be 2.0; for RPM it is calculated and is always somewhat less than 2.0. No values for GASP are shown for r = 18.3 and 23.2 m since this is outside the computational domain.

In Fig. 24 a bar chart is presented showing the comparison of RPM and GASP predictions of impingement pressure with SPIFEX data for the F1F plume (same as F3F plume) as a function of clock angle, ϕ, around the nozzle. For most cases the RPM and GASP values are in good agreement with the data. Test points 56 and 126 show the SPIFEX data higher than either RPM or GASP predictions.

Figure 25 presents the RPM, CART, and USA predicted impingement pressures with SPIFEX measured pressure data for the F1F/F2F dual jet as a function of θ for ϕ = 180°. Three values of r are shown from 9.15 to 15.2 m. In most all cases, there is very good agreement between data and prediction by RPM and the two CFD codes.

Conclusions

This paper has presented sample plume flow fields from Orbiter PRCS jets. Examples were shown of plumes from low scarf-angle single jets, high scarf-angle single jets, zero scarf-angle dual jets, and high scarf-angle single jets. It was seen that results from the JSC RPM engineering model compare well with the flow fields generated from the higher-fidelity GASP, CART, USA, and RAMP CFD codes. The RPM predictions of impingement pressure were shown to compare very well with measured SPIFEX impingement pressures for the low scarf-angle F3U jets and reasonably well with the high scarf-angle F1F and F1F/F2F SPIFEX data. In summary, the plume flow fields from the RPM code appear to be validated satisfactorily to use in prediction of pressure and heating environments to space station components.

Acknowledgments

The authors wish to acknowledge the support of Jeff Arend of the JSC Space Station Office on this project. Thanks are also extended to Jay LeBeau and Steve Fitzgerald of NASA/JSC for plume solutions and comments and to Ruston Hughes and Stan Bouslog (formerly with Lockheed Martin) who helped develop the RPM code.

References

1. Fitzgerald, S. M., Rocha, A. R., Bouslog, S. A., Hughes, J. R., and Leahy, K. S., "Far-Field Plume Characterization Testing in Support of Space Station Plume Impingement Methodology Validation," Paper 94-2636 presented at 18th AIAA Aerospace Ground Testing Conference, Colorado Springs, CO, June 20-23, 1994.

2. Stueber, M. J., "Plume Characterization Test Report for the NASA/JSC Chamber A Vacuum Facility: Vol. I," JSC-32321, Oct. 1994.

3. Fitzgerald, S. M., Bouslog, S. A., and Hughes, J. R., "Model for Predicting Orbiter PRCS Impingement Loads and Heating," JSC-26507, Rev. A, June 1995.

4. Fitzgerald, S. M. and Bouslog, S. A., "Orbiter PRCS Plume Impingement Toolkit: RPM Version 3.0.1," JSC-26583, Rev. A, Sept. 1996.

5. Rochelle, W. C., Hughes, J. R., and Leahy, K. S., "Model for Predicting Orbiter PRCS Plume Heating to International Space Station Alpha (ISSA)," Lockheed AS-107-94, Aug. 25, 1994.

6. Lumpkin, F. E., Stuart, P. C., and LeBeau, G. J., "Enhanced Analyses of Plume Impingement During a Combined CFD and DSMC Methodology," Paper 96-1877 presented at 31st AIAA Thermophysics Conference, New Orleans, LA, June 17-20, 1996.

7. Machin, R. A., Stueber, M. J., Rocha, A. R., Leahy, K. S., Hughes, J. R., White, M. K., Rochelle, W. C., and Fitzgerald, S. M., "Shuttle Plume Impingement Flight Experiment (SPIFEX) Data Reduction, Vol. I - Test Description and Results," JSC 27030, June 1995.

8. Rochelle, W. C., Hughes, J. R., Leahy, K. S., and Fitzgerald, S. M., "Shuttle Plume Impingement Flight Experiment (SPIFEX) - Heat Flux Measurement and Predictions," Paper 96-0349 presented at AIAA 34th Aerospace Sciences Meeting, Reno, NV, Jan. 15-18, 1996.

9. Fitzgerald, S. M., Hughes, J. R, and Leahy, K. S., "Shuttle Plume Impingement Flight Experiment (SPIFEX) - Pressure and Load Plate Measurements," Paper 96-0611 presented at AIAA 34th Aerospace Sciences Meeting, Reno, NV, Jan. 15-18, 1996.

10. Rochelle, W. C., Hughes, J. R., DeVenezia, J., Bouslog, S. A., Leahy, K. S., and Fitzgerald, S. M., "Plume Impingement Heating to International Space Station (ISS)," Paper 95-2132 presented at 30th AIAA Thermophysics Conference, San Diego, CA, June 19-22, 1995.

11. Rochelle, W. C., Hughes, J. R., Kinsey, R. E., and Caram, J. M., "Heat Transfer from Space Shuttle PRCS Plumes to Components of International Space Station," Paper 96-3965 presented at 1996 AIChE/ASME/ANS/AIAA National Heat Transfer Conference, Houston, TX, Aug. 3-6, 1996.

12. Rochelle, W. C., Kinsey, R. E., Ruby, D. G., Stuart, P. C., and Lumpkin, F. E., "Orbiter Exhaust Plume Impingement Effects on International Space Station," Paper presented at 23rd JANNAF Exhaust Plume Technology Meeting, Sunnyvale, CA, April 8-11, 1997.

13. McGrory, W. D., Stack, D. C., Applebaum, M. P., and Walthers, R. W., "GASP Version 2.2 - The General Aerodynamic Simulation Program," AeroSoft, Inc., 1993.

14. Dominik, D., Fu, T., et. al., "Space Shuttle RCS Plume Flow Field," Rockwell International Report SSD95D0163, April 1995.

15. Smith, S. D., "Update to the RAMP2 Computer Program," SECA-FR-93-19, December 1993.

16. Baldwin, B. S. and Lomax, H., "Thin Layer Approximation and Algebraic Model for Separated Turbulent Flows," Paper 78-257 presented at 16th AIAA Aerospace Sciences Meeting, Reno, NV, Jan. 16-18, 1978.

17. Gordon, S. and McBride, B. J., "Computer Program for Calculation of Complex Chemical Equilibrium Compositions, Rocket Performance, Incident and Reflected Shocks, and Chapman-Jouguet Detonations," NASA SP-273, March 1976.

18. Roe, P. L., "Approximate Riemann Solver, Parameter Vectors, and Difference Schemes," *Journal of Computational Physics*, Vol. 43, pp. 357-372.

19. Van Leer, B., "Towards the Ultimate Conservative Difference Scheme V. A Second Order Sequel to Godunov's Method," *Journal of Computational Physics*, Vol. 32, 1979, pp. 101-136.

20. Walatka, P. P. and Buning, P. G., "PLOT3D User's Manual," NASA TM 101067, March 1989.

21. "Tecplot User's Manual - Version 7," Amtec Engineering, Inc., Aug. 1996.

22. Evans, R. M. and Morse, H. L., "Boundary Layer Integral Matrix Procedure BLIMP-J User's Manual," Aerotherm UM-75-64, July 1975.

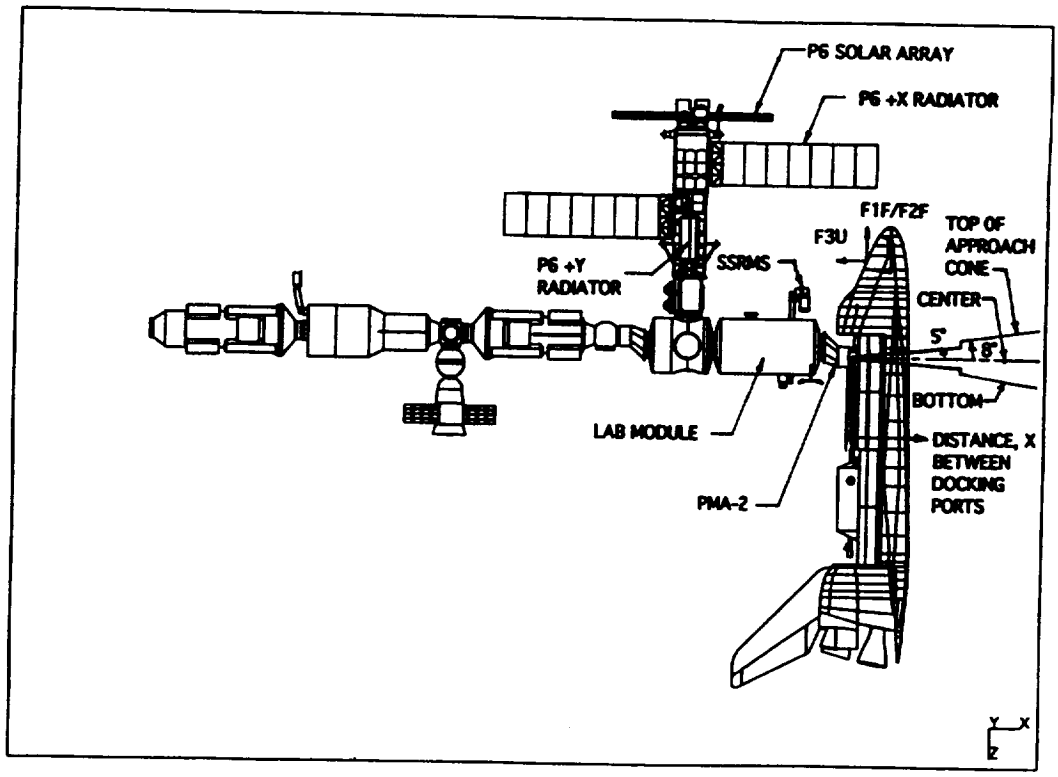

Fig. 1 X-Z Plane View of International Space Station for Flight 6A

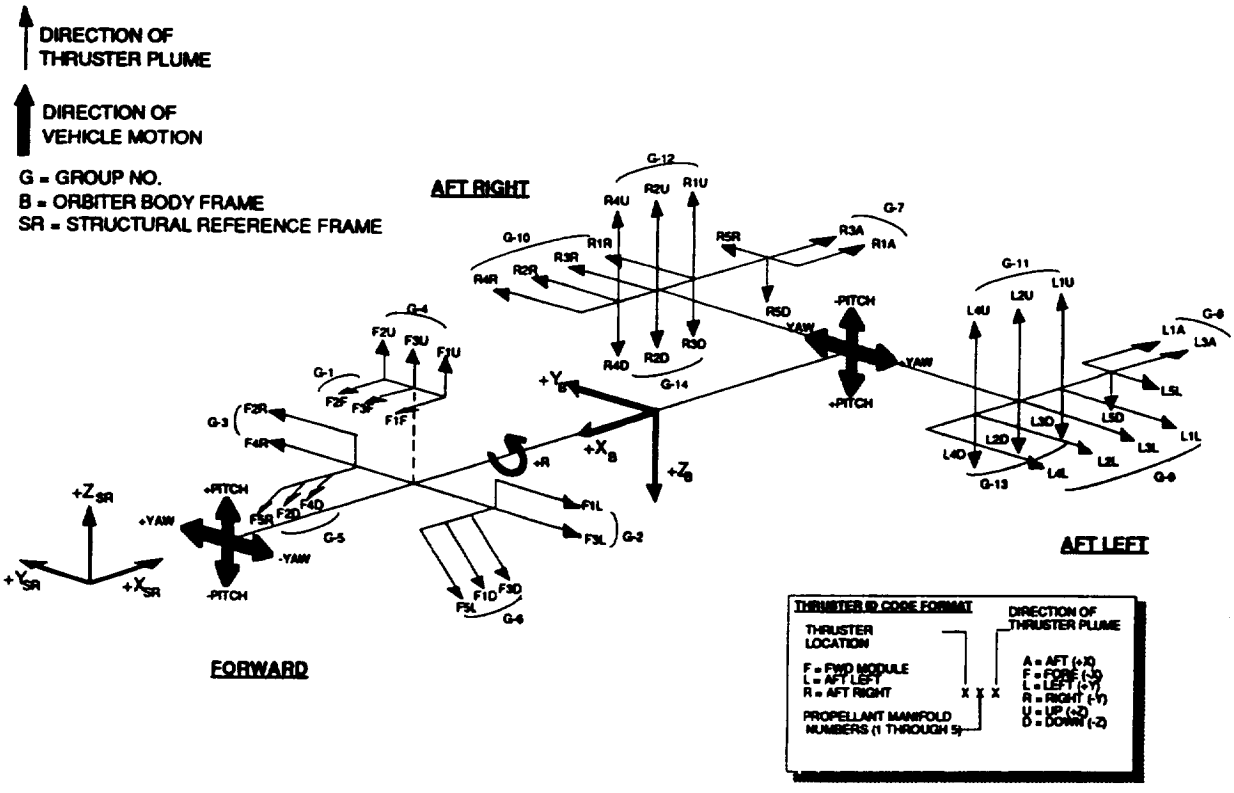

Fig. 2 Orbiter RCS Jet Locations and Plume Directions

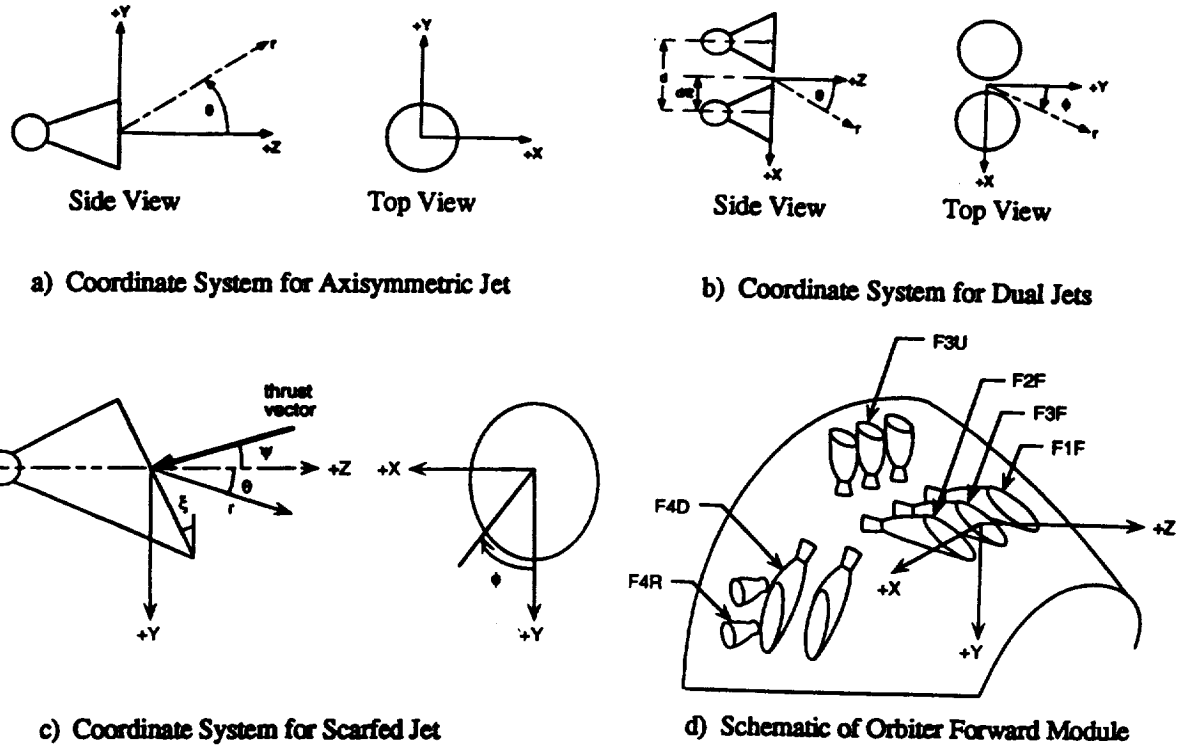

Fig. 3 Orbiter PRCS Jet Coordinate System

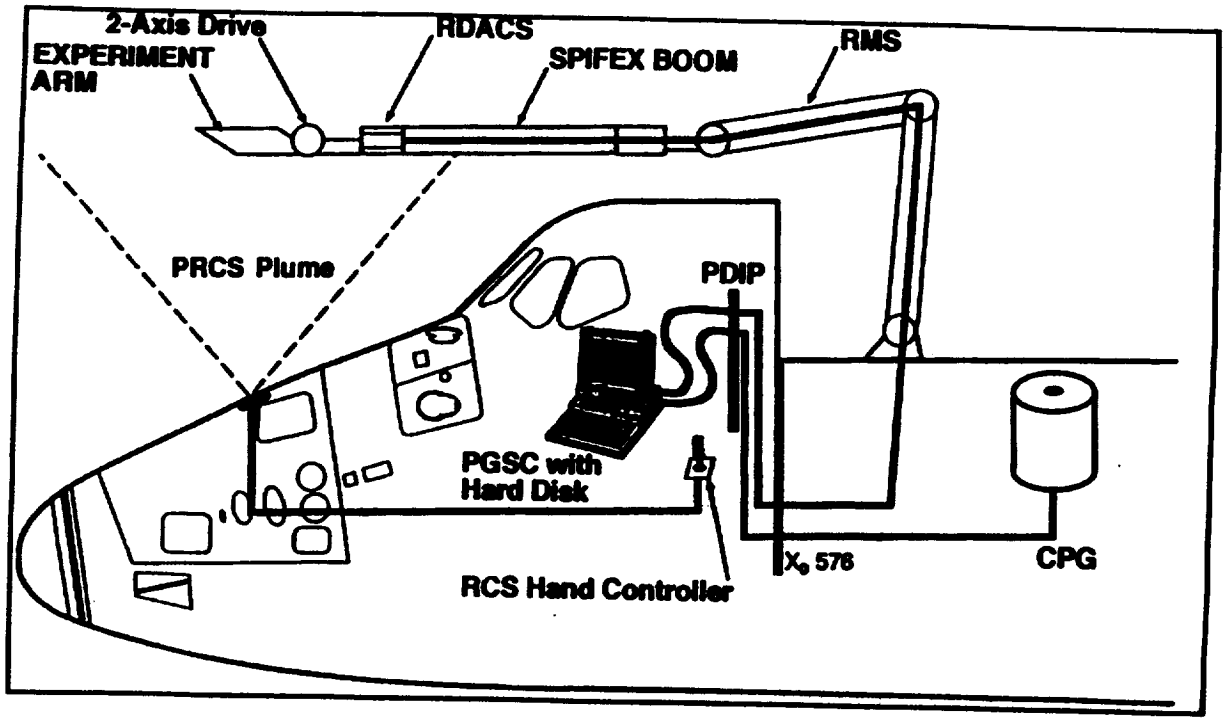

Fig. 4 Overview of Equipment Used for SPIFEX Operations

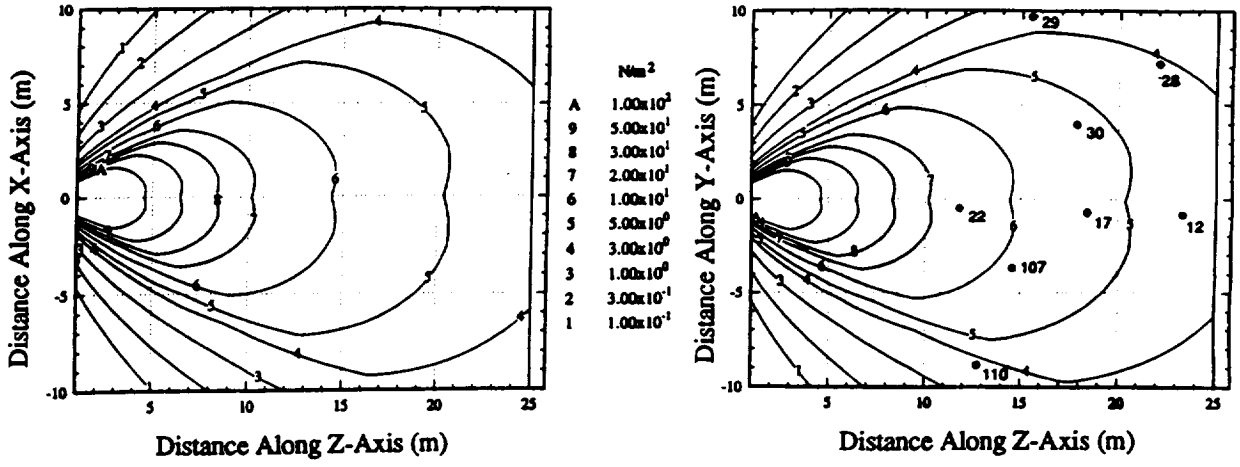

a) X-Z Plane b) Y-Z Plane

Fig. 5 RPM Dynamic Pressure Contours for F3U Single-Jet Plume

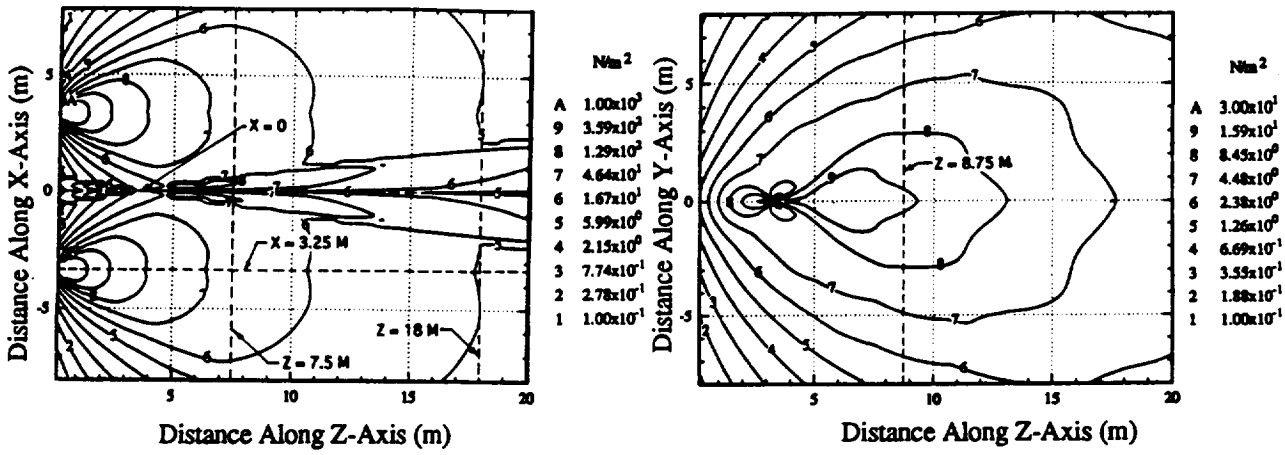

a) X-Z Plane b) Y-Z Plane

Fig. 6 RPM Dynamic Pressure Contours for DTU Dual-Jet Plume

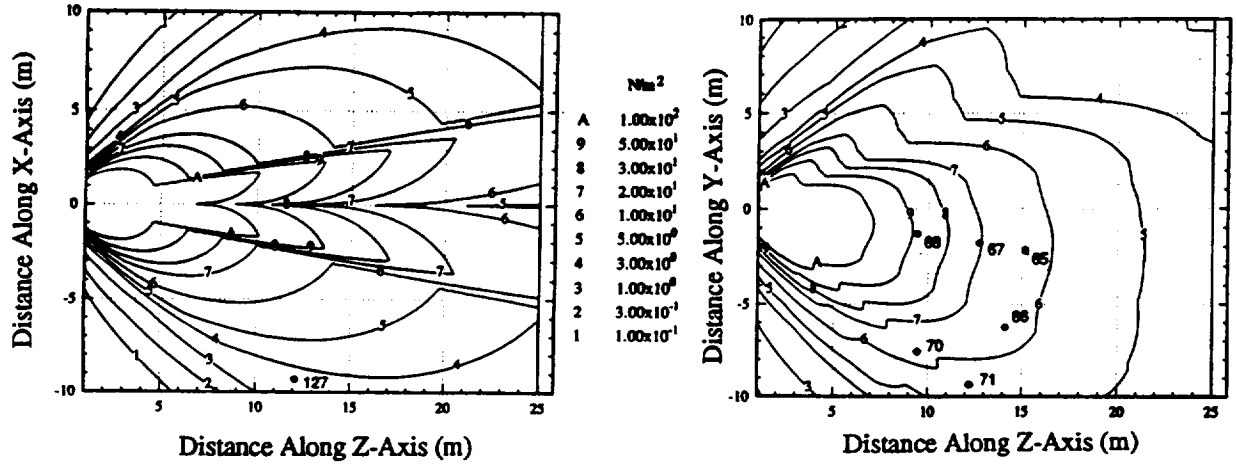

a) X-Z Plane b) Y-Z Plane

Fig. 7 RPM Dynamic Pressure Contours for F1F/F2F Dual-Jet Plume

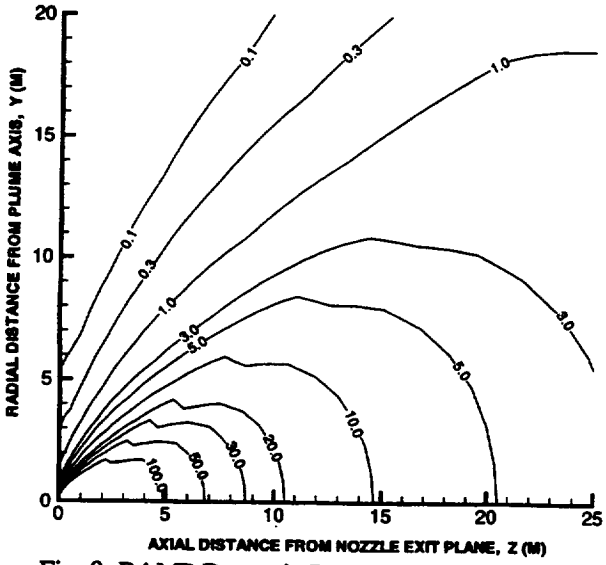

Fig. 8 RAMP Dynamic Pressure Contours (N/m²) for F3U Axisymmetric Plume in Y-Z Plane

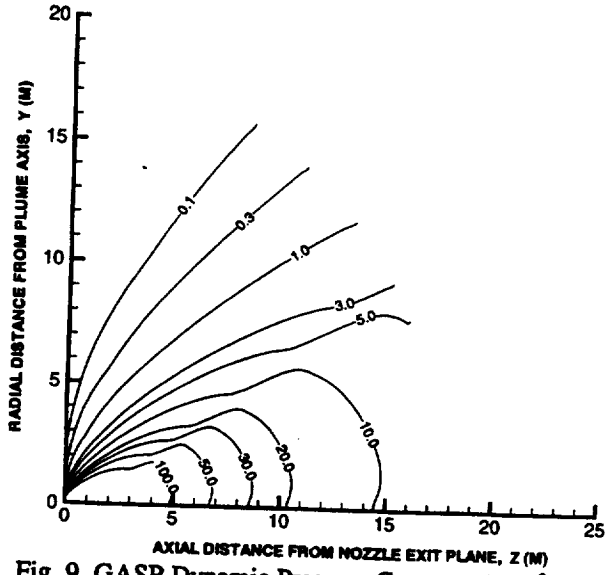

Fig. 9 GASP Dynamic Pressure Contours (N/m²) for F3U Axisymmetric Plume in Y-Z Plane

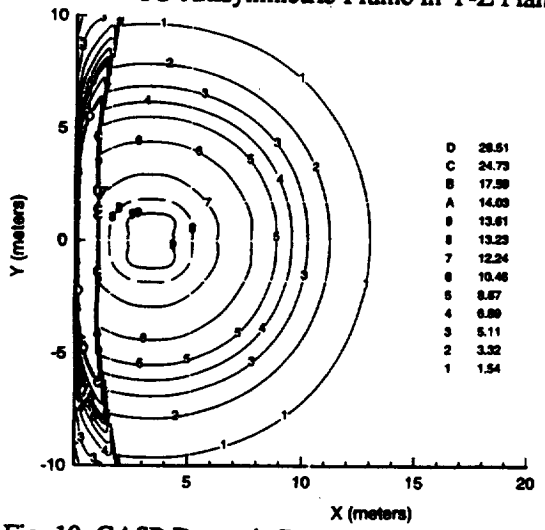

Fig. 10 GASP Dynamic Pressure Contours (N/m²) for DTU Dual-Jet Plume in Y-X Plane (Z=12 m)

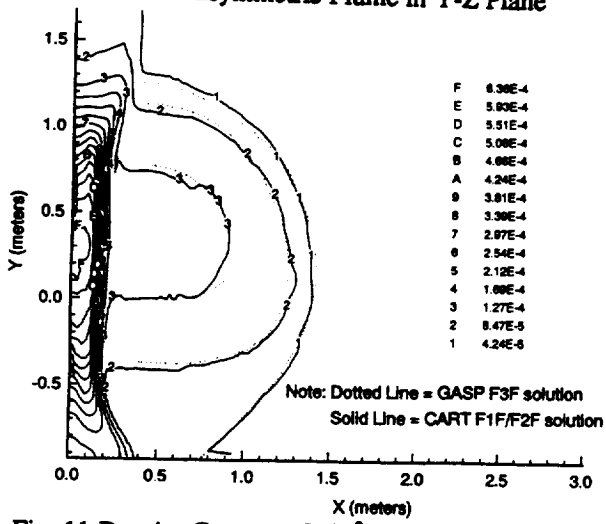

Fig. 11 Density Contours (N/m²) for F3F from GASP and for F1F/F2F from CART (Z=12.0 m)

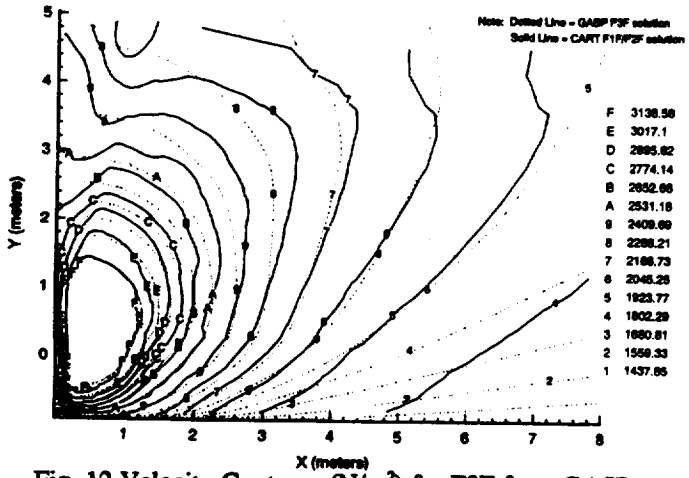

Fig. 12 Velocity Contours (N/m²) for F3F from GASP and for F1F/F2F from CART (Z=12.0 m)

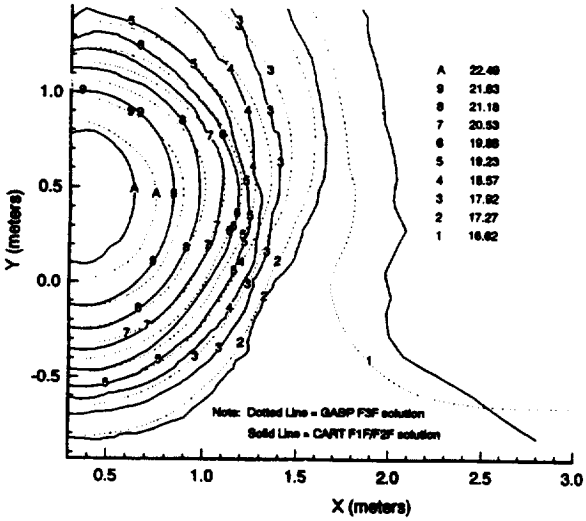

Fig. 13 Molec. Wt. Contours for F3F from GASP and for F1F/F2F from CART (Z=12.0 m)

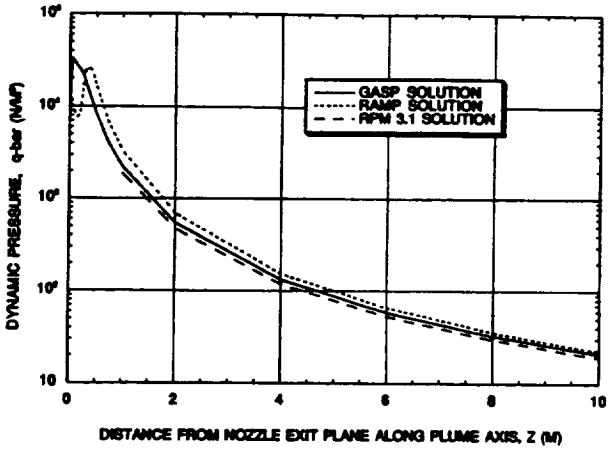

Fig. 14 GASP, RAMP, and RPM F3U Plume Dynamic Pressure vs Z Along Plume Axis

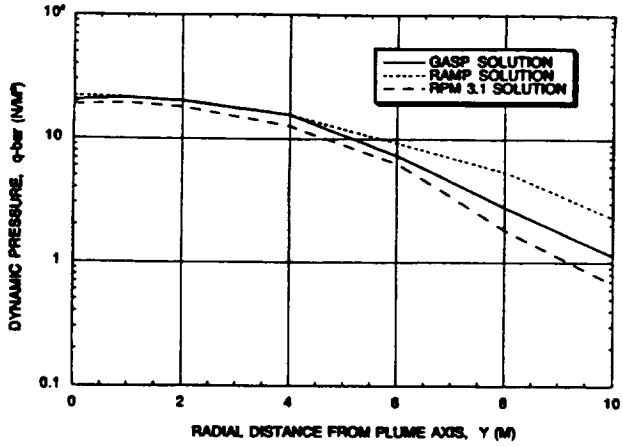

Fig. 15 GASP, RAMP, and RPM F3U Plume Dynamic Pressure vs Y for Z=10 m

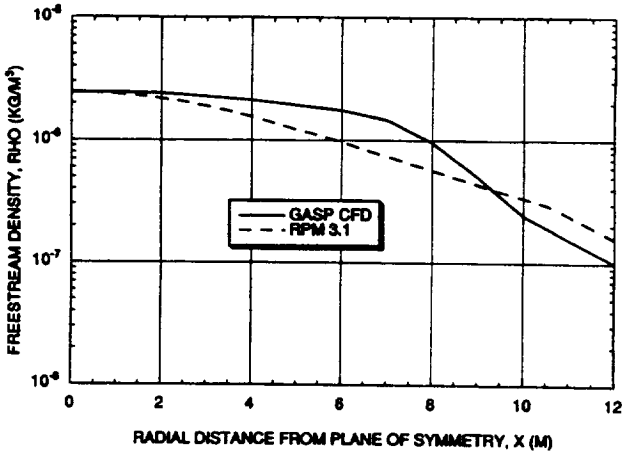

Fig. 16 GASP and RPM F3F Plume Density vs X for Z = 12.5 m and Y=1.0 m

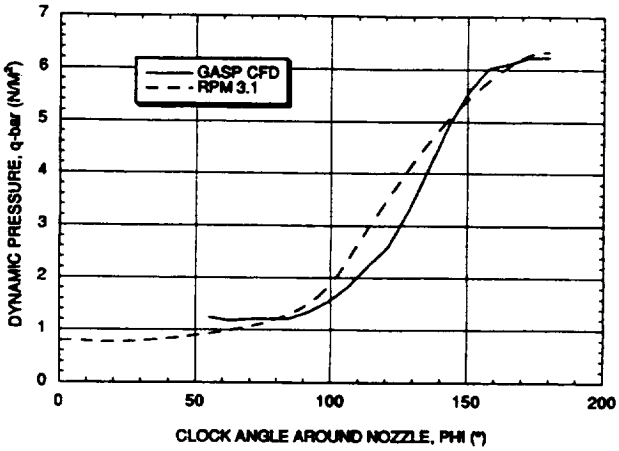

Fig. 17 GASP and RPM F3F Plume Dynamic Pressure vs ϕ at Z=12.5 m and θ=36°

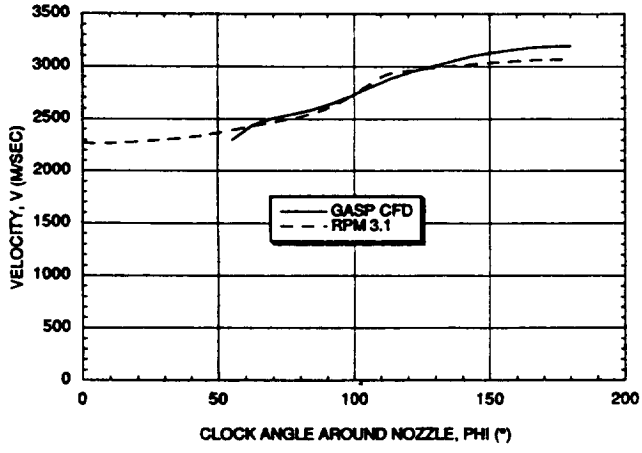

Fig. 18 GASP and RPM F3F Plume Velocity vs ϕ at Z=12.5 m and θ=36°

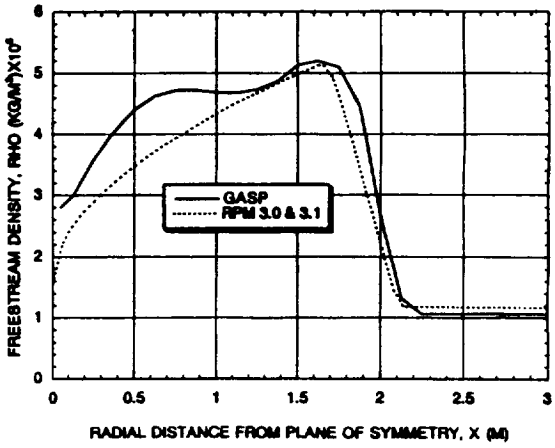

Fig. 19 GASP and RPM DTU Plume Density vs X at Z=18 m

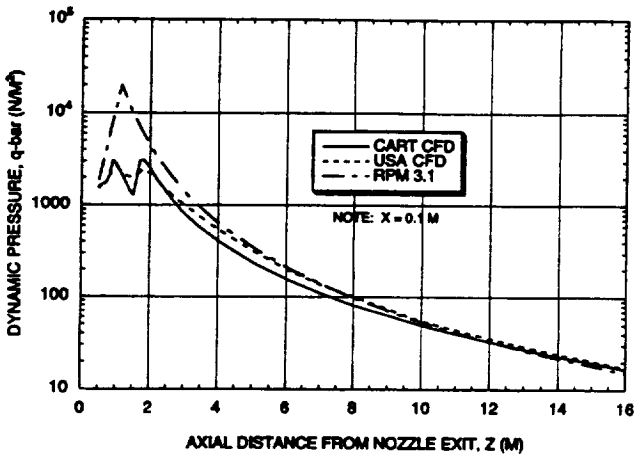

Fig. 20 CART, USA, and RPM F1F/F2F Plume Dynamic Pressure vs Z Along Plume Axis

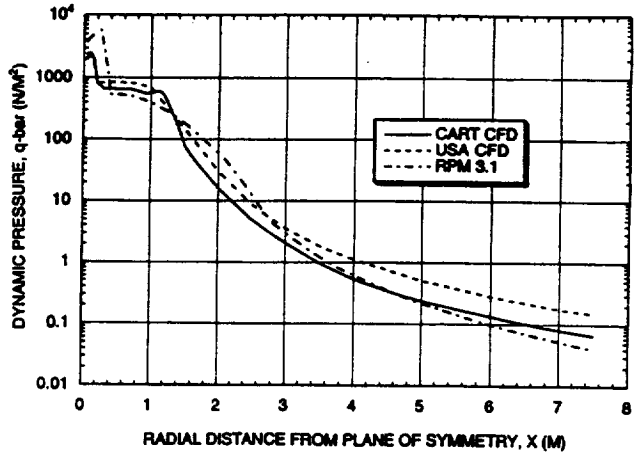

Fig. 21 CART, USA, and RPM F1F/F2F Plume Dynamic Pressure vs X at Z = 2.0 m

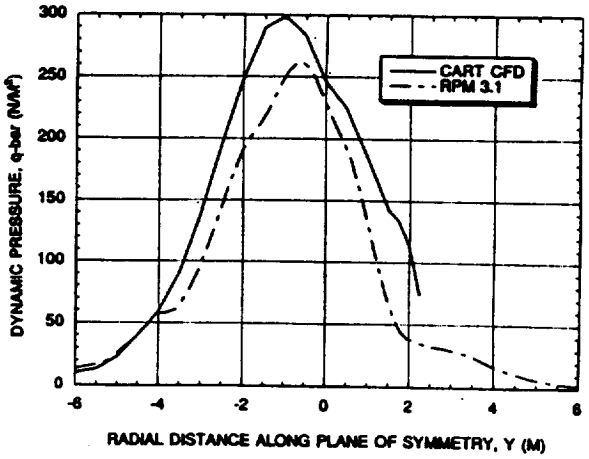

Fig. 22 CART and RPM F1F/F2F Plume Dynamic Pressure vs Y at Z = 5.0 m

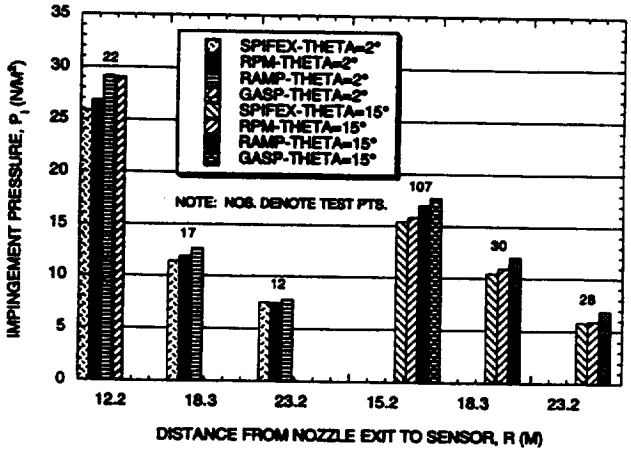

Fig. 23 SPIFEX, RPM, RAMP, and GASP F3U Impingement Pressure vs r for θ = 2° and 15°

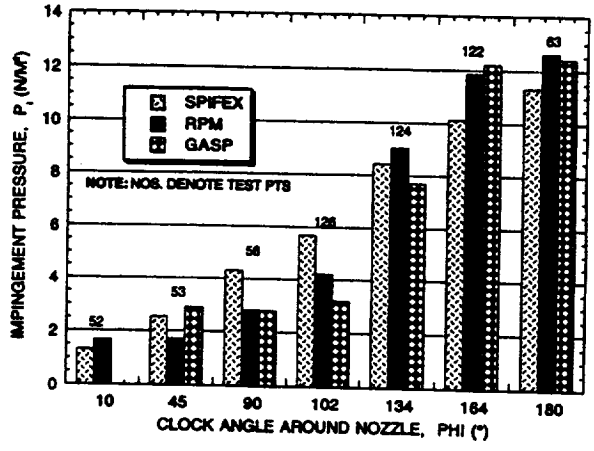

Fig. 24 SPIFEX, RPM, and GASP F1F Impingement Pressure vs φ for r=15 m, θ = 36°

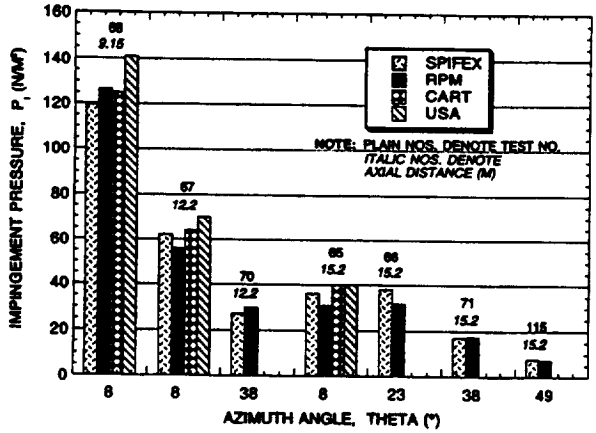

Fig. 25 SPIFEX, RPM, CART, and USA F1F/F2F Plume Impingement Pressure vs θ for r=9.2, 12.2, and 15.2 m